Materials Science & Engineering A 824 (2021) 141819

Contents lists available at ScienceDirect

Materials Science & Engineering A

journal homepage: www.elsevier.com/locate/msea

Probing hydrogen effect on nanomechanical properties of X65 pipeline steel using in-situ electrochemical nanoindentation

Dong Wang [a], Anette Brocks Hagen [b], Di Wan [a], Xu Lu [a,*], Roy Johnsen [a]

[a] Department of Mechanical and Industrial Engineering, Norwegian University of Science and Technology (NTNU), 7491, Trondheim, Norway
[b] SINTEF Industry, 7456, Trondheim, Norway

ARTICLE INFO

Keywords:
Hydrogen embrittlement
Carbon steel
In-situ test
Nanoindentation
Dislocation

ABSTRACT

The hydrogen effect on a X65 carbon steel was investigated using in-situ electrochemical nanoindentation approach. The alterations in elastic behavior, pop-in load, and hardness under hydrogen-free and hydrogen-charged conditions in both ferrite and bainite were compared and discussed. The results demonstrated a non-affected elastic behavior by hydrogen in both microconstituents. The homogeneous and heterogeneous dislocation nucleation are proposed as the dominant mechanisms for pop-in behavior in ferrite and bainite, respectively. In addition, the reduction of pop-in load by hydrogen in both microconstituents indicates a hydrogen-enhanced dislocation nucleation in both homogenous and heterogeneous manners. Moreover, a hydrogen-induced hardness increment was detected in both microconstituents, which is related to the hydrogen-enhanced lattice friction on dislocations. Also, the more prominent hardness increment in bainite was caused by its significantly more trapping sites.

1. Introduction

Carbon steels have been widely used for decades as efficient means for long distance transportation in oil and gas industries due to its low cost, simple manufacture, and remarkable mechanical properties [1]. To date, there are millions of kilometers of pipelines transporting petroleum and natural gases in the world. During these applications, the carbon steels are exposed to a hydrogen-rich environment, either from the contained hydrogen sulfide and hydrogen gas, or from various electrochemical processes such as fuel cell, water electrolysis, and cathodic protection [2,3]. In addition, due to the increasingly urgent demand of energy transition from polluting fossil fuels to clean and renewable energy, the hydrogen energy becomes a very promising candidate due to its overwhelming environmental benefits and high energy efficiency. As a result, an increasing amount of existing, as well as new pipeline networks are applied to transport hydrogen gas [4,5]. However, hydrogen has been widely proposed and documented as a detrimental element for metallic materials, leading to severe degradation of mechanical properties with a catastrophic failure, known as hydrogen embrittlement [6–11]. Thus, the effect of hydrogen on pipeline steels needs further exploration to enable a safe and efficient use for future large-scale hydrogen gas transport applications.

The detrimental effects of hydrogen in iron and steels were first reported in the early 1870s by Johnson [12]. Since then, intensive studies were performed to explain and understand the phenomenon of hydrogen embrittlement, and several mechanisms have been proposed including hydrogen-enhanced localized plasticity (HELP) [13–15], hydrogen-enhanced decohesion (HEDE) [16–20], hydrogen-enhanced strain-induced vacancy formation (HESIV) [8,21–23], adsorption-induced dislocation emission (AIDE) [9], and Defactant mechanism [24–26]. Despite the intensive studies, none of the aforementioned mechanisms can be used to explain all hydrogen embrittlement phenomena exclusively, and these mechanisms also share overlaps with each other. Moreover, a combination of different mechanisms is often applied to explain some complicated hydrogen degradation behavior [6,27]. This is because hydrogen embrittlement is a complex phenomenon that depends heavily on the intrinsic properties of materials, the testing approaches, as well as the applied hydrogen environment. Nevertheless, it has been widely accepted that the interaction between hydrogen and material defects such as dislocations, grain boundaries, vacancies etc. provides a key clue to explain the hydrogen embrittlement behavior.

Up to now, most hydrogen embrittlement studies on carbon steels were performed by using macroscopic mechanical tests on pre-charged

* Corresponding author.
E-mail address: xu.lu@ntnu.no (X. Lu).

https://doi.org/10.1016/j.msea.2021.141819
Received 10 June 2021; Received in revised form 23 July 2021; Accepted 26 July 2021
Available online 27 July 2021

specimens [3,28,29]. These methods can directly show the overall degradation effect of hydrogen on the mechanical properties. However, carbon steels are mainly composed of mixtures of phases and micro-constituents including ferrite, bainite, perlite, and martensite that differ in distribution, volume fraction and relative size whereas the smallest phase and/or constituent can have a major contribution to the final mechanical properties of the steels. The complex microstructure makes the conventional mechanical tests difficult to disclose the intrinsic reaction between hydrogen and material defects. Also, the macroscopic testing methods cannot reveal the hydrogen effect on individual phases, which is very important for the pipeline industries to develop advanced carbon steels by adjusting the volume fraction of each phase to obtain proper mechanical properties as well as a high hydrogen embrittlement resistance. Further, the hydrogen diffusion coefficient in carbon steels with Body Centered Cubic (BCC) structure is 10^4-10^6 times higher than that of Face Centered Cubic (FCC) structure [30]. As a result, a non-negligible amount of dissolved hydrogen can diffuse out during the mechanical tests on pre-charged samples, which makes it difficult to precisely connect the hydrogen degradation effect with the amount of charged hydrogen. Therefore, in order to reveal the hydrogen effect on individual microconstituents under a constant hydrogen concentration, the small-scale nanoindentation test in combination with miniaturized in-situ electrochemical hydrogen charging (ECNI) needs to be carried out. The ECNI technique has been proven as a promising method for probing the hydrogen effect on nanomechanical behavior of metallic materials [31]. By recording high-resolution load-displacement (L-D) data, both the mechanical properties such as elastic modulus and hardness [32–34], and discrete events such as dislocation nucleation, phase transformation, and surface deformation [35–38] can be obtained and detected, and these phenomena have been reported in multi-type of metallic materials. In this study, the in-situ ECNI test was carried out to investigate the hydrogen effect on the nanomechanical response of different microconstituents in the studied carbon steel and thus providing a better fundamental understanding of the associated material degradation mechanisms.

2. Experimental

2.1. Materials and sample preparation

The material examined in the current study is a commercial X65 grade pipeline steel. It was water quenched after austenitizing at 910 °C and followed by a tempering process in a walking beam furnace with a target temperature of 655 °C. The chemical composition is listed in Table 1. The samples were taken from the middle area of a 15.4 mm thick pipe-wall and further cut into round discs with a diameter of 12 mm and a thickness of 2 mm using electrical discharge machining. The sample surface was prepared by mechanical grinding sequentially using 220–4000 grit SiC papers and polishing down to 1 μm diamond spray. For the optical microscopy analysis, the surface preparation was finalized by etching in 3 % Nital solution to reveal the microstructure. While for the ECNI test, the final surface preparation was colloidal silica suspension (OPS) polishing for 20 min to remove the deformation layer and minimize the surface roughness.

Table 1
Chemical composition (wt.%) of the studied X65 steel.

Elements	C	Si	Mn	P	S	Cu	Ni
wt.%	0.07	0.23	1.17	0.01	0.002	0.14	0.15
Elements	Mo	V	Nb	Ti	N	Al	Fe
wt.%	0.13	0.03	0.02	0.002	0.07	0.031	Bal.

2.2. In-situ nanoindentation test

The ECNI test was carried out by using Hysitron Tribo-Indenter TI950 equipped with a long-shaft three-sided pyramidal Berkovich tip, which was specially designed for in-situ tests. An electrochemical cell was integrated for in-situ hydrogen charging, consisting of a platinum counter electrode and a $Hg/HgSO_4$ reference electrode. Hereafter, all the reported potentials in this study are versus this reference electrode. More details related to the in-situ setup can be found in Ref. [39]. The electrolyte used for hydrogen charging was a glycerol-based solution, which contains 600 g borax per liter glycerol. In addition, it was diluted with 20 % distilled water containing 0.002 M $Na_2S_2O_3$ (sodium thiosulfate) to ensure the conductivity and promote hydrogen absorption. The applied electrolyte has been proven as a good candidate for hydrogen charging due to its extremely low oxygen solubility and diffusivity, hence corrosion on the sample surface can be avoided throughout the small-scale in-situ tests [40,41]. The hydrogen charging condition was determined from the polarization curve by polarizing the sample from −2500 to 1500 mV in the same electrolyte with a scan rate of 1 mV/s. In the current study, the charging potential was applied at −1600 mV (the polarization curve is shown in Section 3.2). Moreover, 2 h hydrogen charging was performed before starting the first indentation to ensure a saturated constant hydrogen concentration in the subsurface region. The hydrogen charging was maintained at the same level during the complete test. The load-controlled nanoindentation tests were performed up to a maximum load of 1000 μN at a constant loading rate of 4000 μN/s with a holding time of 0.25 s, followed by an unloading segment until 10 % of the peak value at the same rate with an additional 0.2 s holding segment for drift correction (as shown in Fig. 1). More than 200 indents were performed under both air condition and hydrogen charging condition to guarantee the reproducibility of the results.

2.3. Characterization

Prior to the ECNI test, the microstructure of the studied material was examined by optical microscope and high-resolution scanning electron microscope (SEM, Quanta 650 FEG, Thermo Fisher Scientific Inc.) with a backscattered electron (BSE) detector. Different microconstituents with their volumes were further identified by electron backscatter diffraction (EBSD). Moreover, the electron channeling contrast imaging (ECCI) technique was applied to identify the original dislocation distribution in each microconstituent in detail by controlling the diffraction condition with optimum contrast. As such, the grain matrix can be controlled to show a dark contrast resulting from the “channeling effect”, and the dislocations will be revealed as white curved lines or dots on dark background [42]. The ECCI was performed in the same SEM at an acceleration voltage of 30 kV with a working distance of ~6 mm. After the

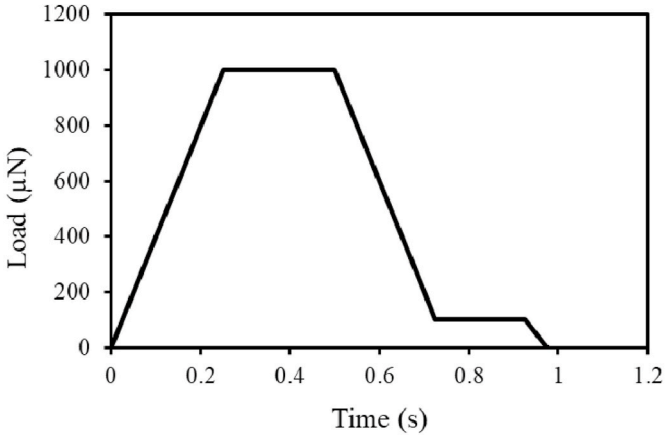

Fig. 1. Load function used for the in-situ nanoindentation test.

ECNI test, all the indents were checked by EBSD and ECCI to select the indents that were performed inside of each microconstituent. The indents that were performed on the grain boundaries or phase boundaries, were eliminated from the results.

2.4. Thermal desorption spectroscopy

The amount of dissolved hydrogen during ECNI experiment was further quantified by the thermal desorption spectroscopy (TDS) analysis. The TDS test was carried out on samples without hydrogen charging and with the same hydrogen charging condition (−1600 mV, 2 h) as in the ECNI test. In order to minimize the hydrogen loss due to the high hydrogen diffusivity in the studied material, the measurement was started immediately (less than 2 min) after the charging and cleaning processes. For the current study, the TDS measurement was performed using Bruker G4 PHOENIX DH with a heating rate of 10 °C/min from room temperature to 700 °C. The amount of hydrogen was further quantified by a mass spectrometry detector (ESD 100, InProcess Instruments, Germany).

3. Results

3.1. Initial microstructure

The microstructure of the tested sample is presented in Fig. 2. The images from optical microscope (Fig. 2a) and SEM (Fig. 2b) show that the material consists of ferrite matrix with bainite laths. Fig. 2c and d are ECCI revealing the details of bainite and ferrite, respectively. Specifically, the bainite consists of clusters of ferrite platelets adjacent to each other with elongated cementite in between. Also, the ECCI in Fig. 2c shows abundant dislocations exist in bainite. In contrast, the dislocation density in ferrite phase is much lower as shown in Fig. 2d. The dislocation density in ferrite phase can be estimated using the two-dimensional approach by counting the number of individual dislocation lines (or dislocation – surface intersections) over the imaging area. It results in a dislocation density of $10^{13}/m^2$ in ferrite phase with an average dislocation space of 330 nm determined by $l_{disl} = \frac{1}{\sqrt{\rho_{disl}}}$. Fig. 2e is the normal direction-inverse pole figure (ND-IPF) map of the studied material, which demonstrates equiaxed grains with an average grain size of 8.5 μm. The blue lines in Fig. 2e represent the low angle grain boundaries with misorientation between 2° and 15°. Combining with the Image Quality (IQ) map in Fig. 2f, the distribution of bainite can be clearly evaluated. The volume fraction of each microconstituents was estimated from the EBSD result, which gives the volume fraction of 24.1 % and 75.9 % for bainite and ferrite, respectively. Fig. 2g is the corresponding Kernel Average Misorientation (KAM) map from the same area. It shows that the local misorientation in the bainite area is higher than the ferrite matrix, indicating a stronger distortion in the bainite microstructure, which is in consistent with the higher dislocation density in bainite than that in ferrite from ECCI results (Fig. 2c and d).

3.2. Polarization curve

The polarization curve of the studied material is shown in Fig. 3. It was scanned from −2500 mV to 1500 mV to determine a proper cathodic potential for hydrogen charging. The curve shows a cathodic branch from −2500 mV till −1250 mV, where hydrogen is produced and

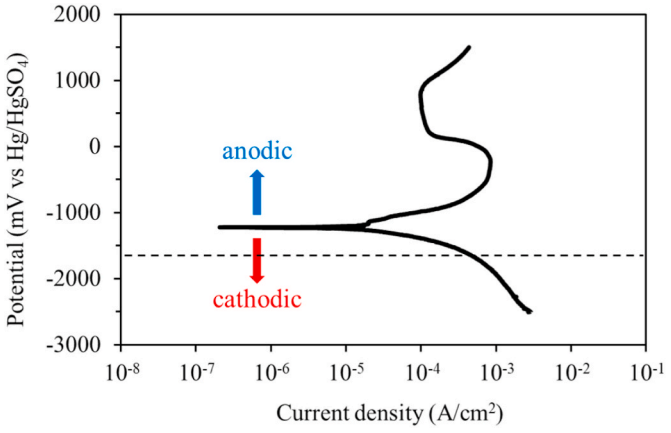

Fig. 3. Polarization curve of the tested X65 sample. The horizontal dashed line indicates the chosen potential for hydrogen charging during ECNI test.

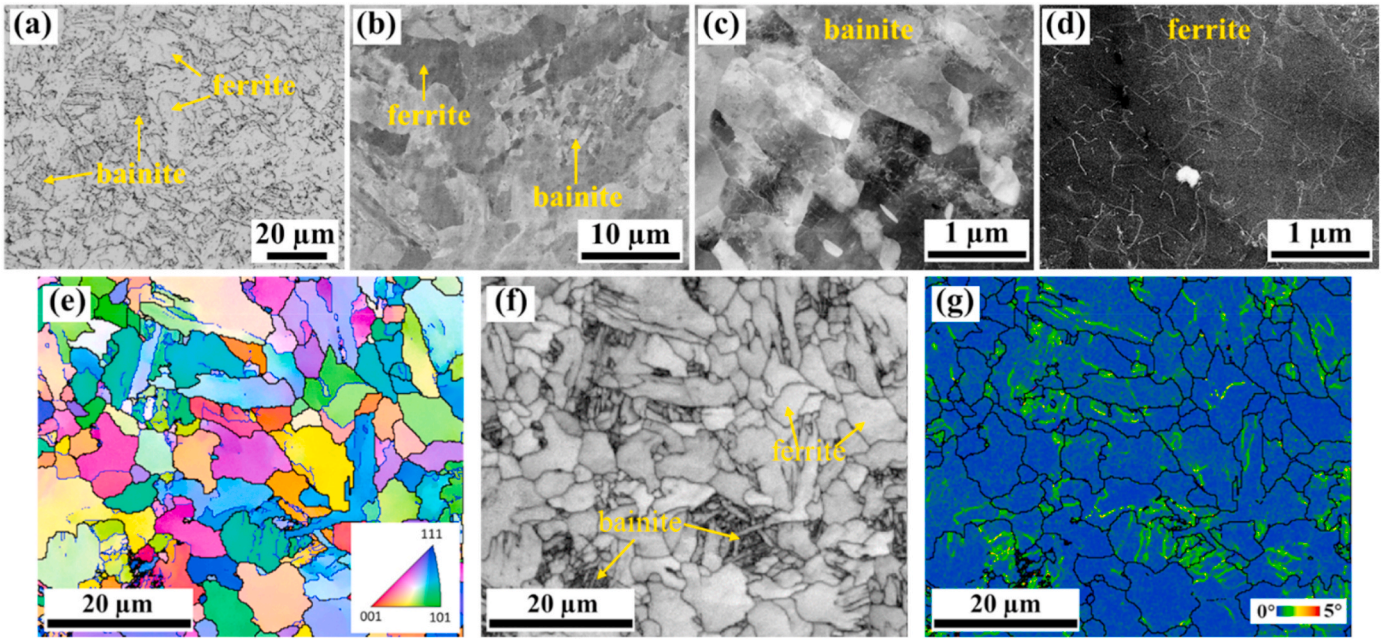

Fig. 2. The microstructure of the tested material. The optical microscopy image (a) and BSE image (b) showing the overall matrix. (c) and (d) are ECCI showing detailed information of bainite and ferrite, respectively. (e–f) are IPF map, IQ map and KAM map in a same area, respectively.

absorbed by the sample surface. In the cathodic polarization, a more negative potential leads to a higher current density, which indicates a higher hydrogen concentration on sample surface during in-situ charging. When the potential is more positive than −1250 mV, the anodic polarization will start. In the anodic branch, a passive zone can be observed between 100 mV and 900 mV, beyond which the trans-passive region will occur. In the current study, the hydrogen charging potential was chosen as −1600 mV (shown as dashed line in Fig. 3). On the one hand, this charging potential will create enough hydrogen on sample surface to reveal the hydrogen effect. On the other hand, −1600 mV is relatively mild to avoid excess hydrogen formation disturbing the sensitive nanomechanical testing.

3.3. In-situ nanoindentation

During a nanoindentation test, a curve showing the applied load as a function of indenting depth (L-D curve) is recorded. Fig. 4 demonstrates the representative L-D curves for ferrite and bainite under both hydrogen-free condition in air and in-situ hydrogen-charged condition. It clearly shows that all curves consist of four stages: initial elastic loading; sudden displacement burst (pop-in); elastoplastic loading; and final elastic unloading. The different segments in a L-D curve can be used to explain different mechanical behavior, which are explained in detail in combination with the comparison of different microconstituents and different hydrogen charging conditions.

3.3.1. Elastic behavior

The first segment of L-D curve demonstrates the elastic loading behavior, which can be used to calculate the reduced elastic modulus E_r. The E_r is a common acquired data from instrumented nanoindentation technique integrated with idealized rigid tips. The conversion between E_r and Young's modulus will be discussed in section 4.1. In the current study, the E_r in different microconstituents under different hydrogen conditions were obtained by fitting the elastic segment with the Hertzian relation [43], which was proposed as:

$$P = \frac{4}{3} E_r h^{3/2} R^{1/2} \tag{1}$$

where P is the applied loading force, h is the indentation depth, and R is the tip radius that equals to 0.9 μm for the current indenter probe. The R value was determined by performing indentation on a standard fused quartz with a defined modulus and calculated by Eq. (1). The relative blunt indenter in this study can be estimated as a sphere tip during the elastic loading area (with a shallow depth of ~10 nm), making the Hertzian fitting more reliable. The average E_r values in ferrite and bainite under hydrogen-free (Air) and hydrogen-charged (H) conditions are presented in Fig. 5. Under the hydrogen-free condition in air, the mean E_r values for ferrite and bainite were 224.8 and 226.9 GPa, respectively. When hydrogen was in-situ charged, the mean E_r values were changed to 222.9 and 228.4 GPa in ferrite and bainite with a change of −0.85 % and 0.66 %, respectively. Given the range of standard deviation, there is no clear difference noticed in the elastic behavior, neither between ferrite and bainite nor under hydrogen-free and hydrogen-charged conditions.

3.3.2. Pop-in

Pop-in, as a sudden displacement burst appearing as a plateau in the L-D curve, is a unique phenomenon and an important parameter for nanoindentation test. Pop-in has been widely reported as a result of dislocation nucleation for ductile metallic materials, indicating the transition from elastic deformation to plastic deformation [31,38,44]. Other mechanisms such as phase transformation or break of surface oxide layer might also be responsible for the pop-in behavior [45,46]. In the current study, the pop-in was observed on all the L-D curves with 100 % probability regardless of the testing condition. Fig. 6 shows the cumulative frequency distribution and the average pop-in load in each condition. Before hydrogen charging, the average pop-in load in ferrite was 340.1 μN, while the pop-in load in bainite was 35.7 % lower as 219.1 μN, as shown in Fig. 6b. When the in-situ hydrogen charging was applied, the pop-in load in both microconstituents were reduced. Specifically, the average pop-in load under hydrogen charging condition was 210.6 and 185.3 μN in ferrite and bainite, respectively. Moreover, it is noticeable that the reduction effect of hydrogen on the pop-in load is more pronounced in ferrite, with 38.2 % reduction compared to 15.4 % in bainite.

3.3.3. Hardness

The hardness value from a nanoindentation test can be determined from the unloading segment of L-D curve by using the Oliver-Pharr method $H = P_{max}/A_c$ [47]. The P_{max} is the maximum load during the indentation, which equals to 1000 μN in this study as shown in the load function in Fig. 1. A_c is the projected contact area that relates to the tip area function and the contact depth h_c. The tip area function for the currently used indenter was calculated as $A_c = 24.5h_c^2 + 1816h_c + 454.1h_c^{1/2}$ by performing tip calibration process on a fused quartz based on the Hysitron TriboIndenter User Manual. The contact depth h_c can be calculated from the maximum indenting depth h_{max} and the stiffness of the unloading curve S as $h_c = h_{max} - 0.75\frac{P_{max}}{S}$. Fig. 7a shows the cumulative frequency distribution of hardness value of ferrite and bainite with/without hydrogen charging. Fig. 7a' demonstrates the mean values

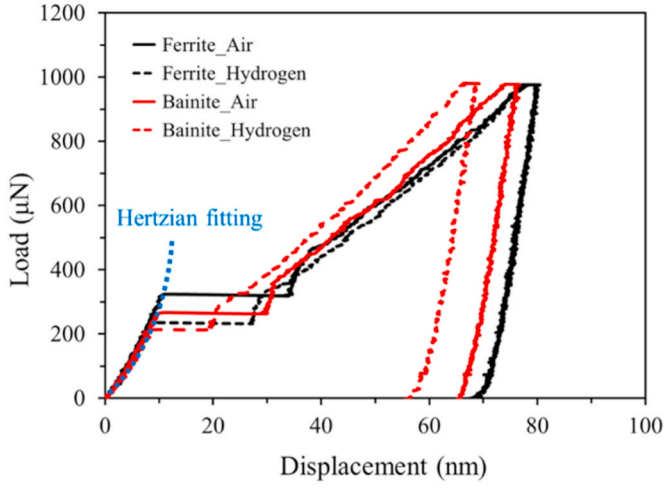

Fig. 4. Representative load-displacement curves for both ferrite and bainite under hydrogen-free (Air) condition and hydrogen-charged condition.

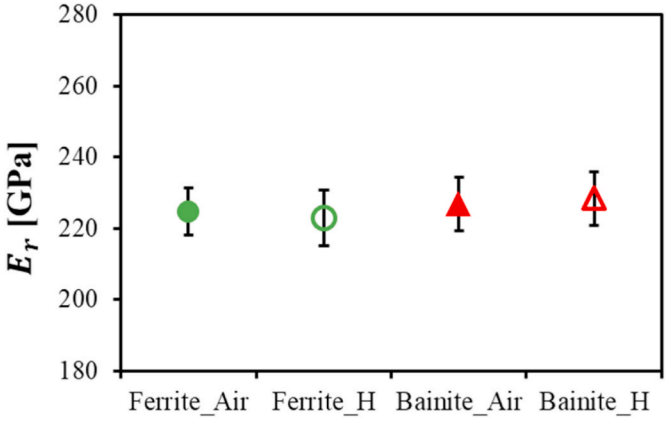

Fig. 5. Reduced elastic modulus for ferrite and bainite obtained by Hertzian fitting under different conditions.

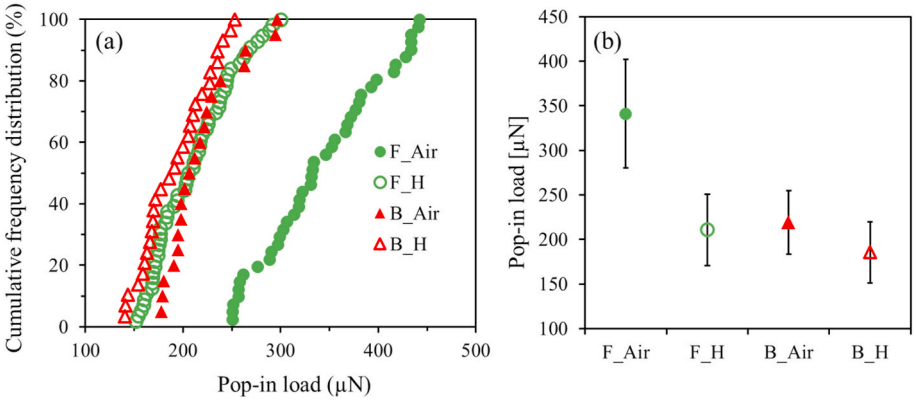

Fig. 6. The cumulative frequency distribution (a) and average value with standard deviation (b) of pop-in load in ferrite (F) and bainite (B) under hydrogen-free (Air) and hydrogen-charged (H) conditions.

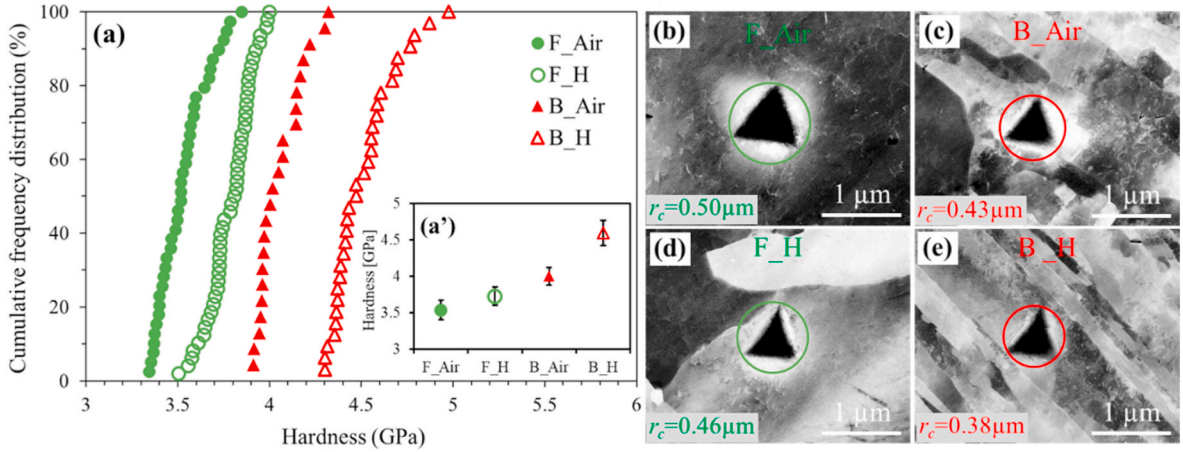

Fig. 7. The cumulative frequency distribution (a) and the average value with standard deviation (a') of hardness in different microconstituents under different conditions. (b)–(e) The representative ECCI of indents in different conditions.

of hardness with their standard deviations in each testing condition, from which two main findings can be detected. Firstly, under hydrogen-free condition in air, the bainite has a hardness value of 4.01 GPa, which is higher than that in ferrite as 3.53 GPa. Secondly, a hydrogen-enhanced hardness behavior is observed in both ferrite and bainite, whereas the increment is more pronounced in the latter one, i.e., the bainite. Upon hydrogen charging, the hardness of ferrite and bainite were 3.72 GPa and 4.60 GPa, with an increase of 5.4 % and 14.7 %, respectively. Fig. 7b–e shows the representative ECCI of the indents with an area dimension close to the average value in different testing conditions. Since all the indentations were performed under the same load function, the difference in the hardness values can also be linked to the residual areas marked as circles around the residual indentation imprints in Fig. 7b–e. From the residual area radius, the harder bainite and softer ferrite, and a hydrogen enhanced hardness behavior in both microconstituents can be easily determined, consistent with the obtained hardness data shown in Fig. 7a.

3.4. Thermal desorption spectroscopy

The TDS test was carried out on two samples, one was in hydrogen-free condition, and the other one was charged with hydrogen under the same electrochemical condition as the performed ECNI test. The TDS results showed a non-detectable hydrogen content in the uncharged sample as 0.00 wppm, while the amount of dissolved hydrogen was detected as 0.335 wppm on the sample after hydrogen charging (−1600 mV, 2 h). In addition, the hydrogen desorption rate in weight ppm per second is calculated and plotted versus the temperature as shown in the grey line in Fig. 8. Due to the overlapping of the detected peaks, the deconvolution process of the TDS spectra is needed to quantitatively

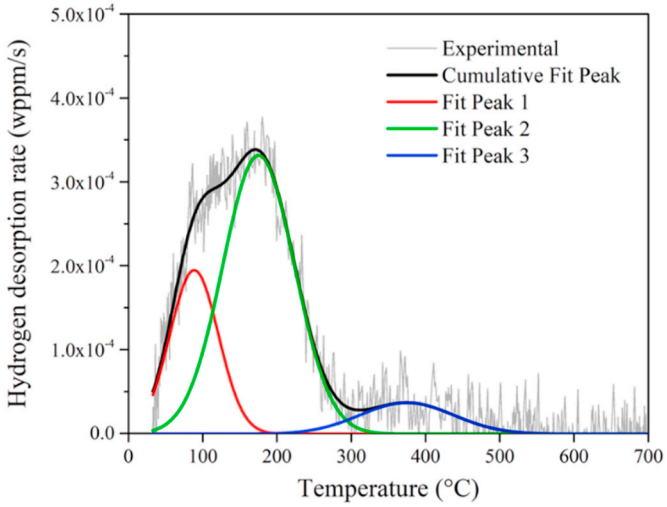

Fig. 8. Deconvolution of the TDS spectra of the tested sample after hydrogen charging (−1600 mV, 2 h) at a heating rate of 10 °C/min.

determine the hydrogen amount in different status. In the current study, the desorption peaks were assumed to follow the Gaussian equation with a symmetric peak shape. As a result, three separated peaks can be derived from the deconvolution process of the original TDS spectra. The black curve in Fig. 8 represents the cumulative curve of these three separated curves and it shows a good fit with the experimental data. Among these three peaks, the first two peaks (red and green curves) deconvoluted from the major peak in the hydrogen desorption signal are diffusible and reversibly trapped hydrogen, respectively. This can be proven by their relatively low peak temperature, which is 91.6 °C for the first peak and 177.9 °C for the second peak, close to other TDS results reported on pure iron with a similar BCC structure [48]. While the third peak under a higher peak temperature of 383.7 °C represents the irreversibly trapped hydrogen.

The amount of hydrogen in different dissolving status can be calculated based on the corresponding area fraction under each peak. The corresponding hydrogen contents in each status are thereby calculated and summarized in Table 2. From Table 2, it clearly shows that the primary dissolved hydrogen is reversibly trapped hydrogen, which is 0.22 wppm and accounts for 66.2 % of the overall hydrogen. While the diffusible and irreversibly trapped hydrogen are 0.083 and 0.03 wppm, as 24.8 % and 9.0 % of the overall dissolved hydrogen, respectively.

4. Discussion

4.1. The effect of hydrogen on elastic behavior

The reduced modulus E_r in both ferrite and bainite under hydrogen-free and hydrogen-charged conditions have been summarized in Fig. 5. In this case, the elastic modulus can be converted from the corresponding E_r value by the following Eq. (2) [43]:

$$\frac{1}{E_r}=\frac{\left(1-\nu_1^2\right)}{E_1}+\frac{\left(1-\nu_2^2\right)}{E_2} \tag{2}$$

here, E is the elastic modulus, ν is the Poisson's ratio, and the superscript numbers 1 and 2 indicate the values for tested material and diamond indenter, respectively. For the applied diamond indenter, the elastic modulus is 1140 GPa and the Poisson's ratio is 0.07 [49]. The Poisson's ratios for both ferrite and bainite were adopted as 0.25 here according to the previous study [50]. Then the elastic modulus in both microconstituents under different test conditions are summarized in Table 3. Prior to hydrogen charging, the elastic modulus of ferrite is calculated as 262.2 GPa, which is very close to that of bainite as 265.2 GPa. Such minor difference in elastic modulus between ferrite and bainite has also been reported in similar ferrite–bainite dual-phase steels via indentation tests [50,51]. When hydrogen is introduced, the elastic modulus of ferrite decreased to 259.4 GPa with a reduction of 1.04 %, while it increased to 267.5 GPa in bainite with an increment of 0.84 %. Though different changes were observed here on the elastic modulus by hydrogen charging, when taking the standard deviation, which is between ±2.37 % to ±2.83 %, into consideration, the effect of hydrogen on the elastic modulus is almost negligible.

In fact, the effect of hydrogen on the elastic behavior is still under debate. Shalskyi et al. [52] investigated the effect of hydrogen on elastic modulus of a low carbon steel using a time-of-flight approach. It detected an increased speed of sound when hydrogen is charged, indicating a hydrogen-enhanced elastic modulus behavior. On the other hand, electrochemical nanoindentation study on Ni–Cr bi-alloys and 316L stainless steel showed a negligible hydrogen effect on the elastic behavior [53]. This observation is in consistence with the conclusion from Zhang et, al. [54], who measured the change of elastic modulus of α-Fe induced by hydrogen using a Bordoni type apparatus and found that 7 to 8 wppm hydrogen does not change the elastic modulus. In contrast, a reduction effect of hydrogen on the elastic modulus was also reported in several studies. Lunarska et al. [55] found that hydrogen decreases the shear modulus as well as Young's modulus of ultra-pure iron at low temperature (90–200 K). Muller et al. [56] reported a hydrogen-reduced elastic modulus on pure nickel by approximately 15–20 % using a novel nanoindentation test with backside exposed to in-situ hydrogen charging. Moreover, Ortiz et al. [57] measured the effect of hydrogen on elastic modulus of martensitic steel and low carbon steel by means of the classical resonant bar method and concluded that hydrogen decreases the elastic modulus of both steels. Despite the aforementioned controversial findings, which indicate a non-universal hydrogen effect on the elastic behavior, hydrogen shows no effect on the elastic behavior in the current study given the range of standard deviations. This is probably due to the applied mild hydrogen charging condition in combination with the relative low hydrogen solubility in BCC structured carbon steel, leading to a low amount of dissolved hydrogen (0.335 wppm from the TDS analysis). As a result, the elastic modulus associated with the interatomic cohesive force does not change by this limited amount of hydrogen. In the current study, the impact of hydrogen mainly focuses on the plastic behavior, which will be discussed in the following sections.

Table 2
Hydrogen concentration according to the peak deconvolution.

	Peak1	Peak2	Peak3
H percentage	24.8 %	66.2 %	9.0 %
H content [wppm]	0.083	0.22	0.03
Peak temperature [°C]	91.6	177.9	383.7
H status	Diffusible	Reversibly trapped	Irreversibly trapped

Table 3
The elastic modulus in hydrogen-free and hydrogen-charged conditions.

Condition	Microconstituents	Mean elastic modulus (GPa)	Standard deviation
H-free	Ferrite	262.2	±6.2 (2.37 %)
	Bainite	265.2	±7.2 (2.70 %)
H-charged	Ferrite	259.4	±7.3 (2.83 %)
	Bainite	267.5	±7.0 (2.62 %)

4.2. The effect of hydrogen on dislocation nucleation

The pop-in phenomenon, as a sudden displacement excursion in L-D curves under load-controlled test mode, may occur either by intrinsic effects such as dislocation nucleation and phase transformation [49,58], or by extrinsic reasons such as oxide film breaking and surface contaminations [59]. In the current study, dislocation nucleation is the only possible mechanism responsible for the pop-in behavior, and the other mechanisms can be excluded since the studied material has a stable phase with a careful surface preparation before test. The dislocation nucleation can either be homogeneous dislocation nucleation from an initial defect-free volume or heterogeneous dislocation nucleation with a nucleation source of pre-existing defects [45,60]. To determine the possible dislocation nucleation mechanisms responsible for pop-ins, the corresponding length scale d_a representing the activation volume at the onset of pop-in needs to be assessed. When a pop-in occurs, the stress distribution beneath the indenter can be estimated according to the continuum mechanics, which gives the value τ_{max} and position $Z_{\tau(max)}$ of the maximum shear stress by Ref. [43].

$$\tau_{max}=0.31\left(\frac{6{E_r}^2}{\pi^3R^2}P\right)^{\frac{1}{3}} \tag{3}$$

$$Z_{\tau(max)}=0.48a_c=0.48\left(\frac{3PR}{4E_r}\right)^{\frac{1}{3}} \tag{4}$$

Here a_c is the contact radius, P is the applied load when pop-in occurs, and R is the radius of tip curvature equals to 0.9 μm as shown in Eq. (1). Since the maximum shear stress occurs at a point beneath the indenter,

different models have been proposed to estimate the activation volume and its corresponding length scale and were summarized by Zhao et al. [60]. In the current study, the volume where the shear stress is higher than 98 % of the maximum shear stress was assumed as the activation volume, according to the model proposed in Ref. [61]. This results in a semi-elliptical region with a major axis of 0.29 a_c, which was chosen as the activation length scale d_a. The a_c value was calculated to be 97.4 nm and 83.4 nm for ferrite and bainite in air condition, respectively. This results in a corresponding d_a of 28.2 nm for ferrite and 24.2 nm for bainite. It needs to be mentioned here that other models summarized in Ref. [60] were also used, resulting in similar d_a values in the range of tens of nm, which will not affect the discussion below.

The mean spacing between dislocations l_{disl} can be estimated from 2D dislocation density ρ_{disl} ($l_{disl} = \frac{1}{\sqrt{\rho_{disl}}}$) based on the ECCI shown in Fig. 2. In ferrite, the l_{disl} is calculated as 330 nm, while the dislocation density in bainite is significantly higher than that in ferrite with several orders, making the l_{disl} estimation impractical from ECCI. In the present study, the indentation is randomly applied on the sample surface and the probability of probing on a region with a pre-existing dislocation is low in ferrite. Therefore, the pop-in phenomenon in ferrite is mainly due to homogeneous dislocation nucleation. Moreover, the shear modulus μ is calculated in ferrite by $\mu = \frac{E}{2(1+\nu)}$ and it has a relation with τ_{max} from Eq. (3) as $\tau_{max} = \mu/19$. This is exactly in the range of $\mu/20$ to $\mu/10$, as proposed for homogeneous dislocation nucleation by the Frenkel model [62]. In bainite, on the other hand, the observed pop-in is suggested to be caused by heterogeneous dislocation nucleation. This is due to the fact that the mean spacing between dislocations in bainite is much smaller than the activation volume dimension, enabling a significantly high possibility for the tip to probe into a volume with pre-existing dislocations or vacancies. Hence, the homogeneous dislocation nucleation is responsible for pop-ins in ferrite, while the heterogeneous dislocation nucleation is responsible for pop-ins in bainite. This conclusion is also consistent with other studies [45] proposing that a higher content of defects leads to a higher probability to trigger a heterogeneous dislocation nucleation.

It has been claimed that heterogeneous dislocation nucleation can be initiated at relatively low stress compared with homogeneous dislocation nucleation, due to the aid from pre-existing defects in the onset process [60,63]. In other words, the activation energy needed to nucleate a dislocation homogeneously is higher than heterogeneously. The activation energy ΔG for homogeneously nucleating a dislocation with radius r is proposed by the classic dislocation theory as [64].

$$\Delta G = 2\pi r W_{dis} - \pi r^2 b \tau_{max}, \tag{5}$$

where W_{dis} is the line energy of the newly formed dislocation loop and b is the Burgers vector of the dislocation as 0.25 nm W_{dis} can be calculated by the following relation [45,65]:

$$W_{dis} = \frac{2-\upsilon}{1-\upsilon}\frac{\mu b^2}{8\pi}\left(\ln\frac{4r}{r_{core}} - 2\right), \tag{6}$$

where υ is the Poisson's ratio, μ is the shear modulus, and r_{core} is the dislocation core radius ($\sim b$). $2\pi r W_{dis}$ in Eq. (5) represents the line energy of the formed dislocation loop, and $\pi r^2 b\tau_{max}$ represents the work needed for expanding the dislocation loop. Therefore, a sufficiently high τ_{max} is needed to initiate a dislocation embryo in defect-free region and grow to the critical radius r_c, where ΔG has a maximum value ΔG_c as nucleation barrier at $d\Delta G/dr_c = 0$. It has been proposed that an initial nucleated dislocation embryo must overcome the energy barrier and grow pass the critical radius to become a perfect dislocation loop with maximum slip vector reaching to that of the Burgers vector [44,66]. Otherwise, the initial dislocation embryo will shrink and vanish. On the other hand, due to the pre-existing dislocations or vacancies as the nucleation sites, the heterogeneous dislocation nucleation may prevail at a relatively low stress compared with homogeneous dislocation nucleation, which is also supported by other studies focusing on the pop-in behavior [63,67]. As a result, the pop-in responsible for homogeneous dislocation nucleation should occur at a higher load than that for heterogeneous dislocation nucleation. This is exactly what has been observed in the current study, where the pop-in load in ferrite is 35.7 % higher than the pop-in load in bainite before hydrogen charging as shown in Fig. 6.

In ferrite, the shear modulus is 104.9 GPa and 103.8 GPa in hydrogen-free and hydrogen-charged condition from Eq. (2) and the corresponding average τ_{max} is thereby calculated as 4.8 GPa and 4.2 GPa in hydrogen-free and hydrogen-charged condition from Eq. (3), respectively. Then the formation energy ΔG can be plotted as a function of loop radius normalized by the Burgers vector r/b as shown in Fig. 9. It shows that the energy barrier (ΔG_c) in the hydrogen-free condition is below 0 eV, indicating a spontaneous homogeneous dislocation nucleation at the applied shear stress. In other words, the pop-in behavior should occur at the applied pop-in load, and this is exactly what was observed in the experiment. In contrast, the free energy curve in hydrogen-charged condition shows a relatively high activation energy above 0 eV, indicating that the dislocation nucleation behavior is energetically unfavorable and there should be no pop-in behavior at the applied load. However, this is inconsistent with experimental observation, where a clear pop-in was detected at the applied load. Therefore, this energy barrier must be overcome during the indenting process to nucleate a dislocation under the applied stress. Since the free energy calculation in Eq. (5) did not take intrinsic hydrogen effect into consideration, which was the only difference between the tests in hydrogen-free and hydrogen-charged conditions. The hydrogen, as a result, is the only possible explanation for the reduction of the energy barrier. In addition, according to the Defactant theory proposed by Kirchheim [25,26], the dissolved hydrogen can act as defactants and reduce the formation energy of defects. In this regard, the dissolved hydrogen can segregate around the dislocations and effectively increase the loop radius. As a result, the dislocation line energy and the corresponding free energy are both reduced based on Eqs. (5) and (6). Therefore, the homogeneous dislocation nucleation in ferrite is enhanced by the dissolved hydrogen with a relatively low pop-in load in the hydrogen-charged condition. Recently, the hydrogen effect on dislocation behavior was examined by Yu et al. [68] using the three dimensional discrete dislocation plasticity simulations on microcantilevers in iron. It was found that hydrogen promotes dislocation generation at relatively low concentration of 0.1 appm, which is typical for BCC materials, owing to the hydrogen shielding effect. This simulation outcome strongly supports the observed hydrogen-reduced pop-in behavior in the current study. Moreover, the hydrogen-reduced pop-in

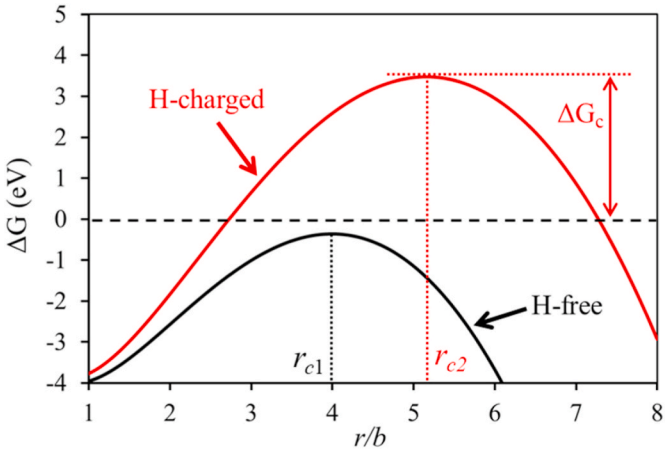

Fig. 9. Free energy for homogeneous dislocation nucleation as a function of the dislocation loop radius in hydrogen free and hydrogen-charged conditions in ferrite.

load behavior can also be explained by showing the relation between the pop-in load P and energy barrier at r_c where $d\Delta G/dr_c = 0$ by combining Eqs. (3) and (5) as:

$$P = \left(\frac{W_{dis}}{r_c}\right)^3 \frac{\pi^3 R^2}{0.178\, b^3 E_r^2}, \tag{7}$$

When hydrogen is introduced, the dislocation line energy W_{dis} will be reduced due to an increased core radius based on Eq. (6), while the critical loop radius r_c will be increased as shown in Fig. 9. As a result, the pop-in load in the hydrogen-charged condition is lower compared to the hydrogen-free condition.

In bainite, where the heterogeneous dislocation nucleation is responsible for the pop-in phenomenon, the pop-in load is also reduced by the dissolved hydrogen as shown in Fig. 4. Two proposed mechanisms can be used to explain this behavior. The first one is the hydrogen-enhanced vacancy-mediated heterogeneous dislocation nucleation [69], which suggests that the heterogeneous dislocation nucleation is governed by a vacancy or vacancy cluster related process through agglomeration and collapse of vacancies into the plates on densely packed planes. When hydrogen is charged into the material, the interaction between hydrogen atoms and vacancies would result in a higher equilibrium vacancy concentration by reducing their formation energy. Thus, the hydrogen enhanced vacancies and vacancy clusters can reduce the required stress for the onset of plastic deformation. As a result, the pop-in related to heterogeneous dislocation nucleation occurs at a lower load upon hydrogen charging. This mechanism is supported by the atomistic simulation showing a reduction in stress for incipient plastic deformation by vacancies [70]. The other possible mechanism proposes that the interstitial dissolved hydrogen can act as stress concentrator and contribute to the pop-in behavior underneath the indenter, leading to a significantly reduced stress for heterogeneous dislocation nucleation [71]. To summarize, the pop-in events in ferrite correspond to homogeneous dislocation nucleation, which needs a higher triggering stress than that for heterogeneous dislocation nucleation governed pop-in in bainite. Also, the pop-in loads for both cases are reduced by dissolved hydrogen.

4.3. The effect of hydrogen on hardness

Prior to hydrogen charging, the L-D curves obtained in bainite exhibit a smaller maximum displacement (Fig. 4) with a smaller residual indent area (Fig. 7) compared with those in ferrite. This indicates that the original hardness in air condition in bainite is higher than that in ferrite, as shown in Fig. 7a. This can easily be explained by the microstructure of bainite, which is recomposited from austenite at a proper temperature and cooling rate where its thermodynamics is unstable. As a result, the bainite, with a fine plate-like microstructure, consists of cementite and dislocation-rich ferrite. The harder cementite, the high dislocation density in ferrite present in bainite, and its fine platelet size, make the bainite intrinsically harder than ferrite [72].

The elastoplastic regime of the L-D curve describes a continuously hardening process during the indentation. By using the definition of hardness $H = P/A_c$ and the Tabor relation-based Nix-Gao model [73], the elastoplastic regime of the L-D curve can be derived as:

$$P = H_0 A_c = C\sigma A_c \tag{8}$$

where H_0 is the depth-dependent hardness during the elastoplastic regime, $C \approx 3$ is the Tabor factor, and σ is the flow stress. In the current study, the flow stress σ consists of Taylor stress σ_{Taylor} due to the dislocation interaction, lattice friction stress σ_{Fric}, and the stress caused by grain boundaries and phase boundaries $\sigma_{boundary}$. Among them, the Taylor stress can be described by the Taylor relation as

$$\sigma_{Taylor} = M\alpha\mu b\sqrt{\rho_{SSD} + \rho_{GND}} \tag{9}$$

Here, the $M \approx 3.06$ as the Taylor factor relates the shear flow stress to the tensile flow stress. α is an empirical factor depending on the dislocation structure. ρ_{SSD} and ρ_{GND} are the density of statistically stored dislocation (SSD) and geometric necessary dislocation (GND) within the indented plastic zone, respectively. The ρ_{SSD} is the original dislocation density distributed in the sample before test, and the ρ_{GND} relates to the shape of indenter, plastic zone size, and indentation depth. By combining Eqs. (8) and (9), the elastoplastic regime indicating continuous hardening behavior can be described as follows.

$$P = CM\alpha\mu b A_c\sqrt{\rho_{SSD} + \rho_{GND}} + C\left(\sigma_{Fric} + \sigma_{boundary}\right)A_c \tag{10}$$

The harder bainite and softer ferrite can also be explained by Eq. (10), where the main different parameters between these two microconstituents when indenting to the same depth are ρ_{SSD}, σ_{Fric}, and $\sigma_{boundary}$. Specifically, the bainite has an initially higher dislocation density as shown in Fig. 2 resulting in a relatively high ρ_{SSD}; the σ_{Fric} in bainite is also higher than in ferrite due to the contained cementite in bainite, leading to a higher friction to dislocation motion. In addition, the data in ferrite are selected to avoid the influence from grain boundaries (by checking the SEM images of the area after indentation), while the bainite contains small lath size making all indents inevitably hitting the lath boundary. Thus, the $\sigma_{boundary}$ in ferrite can be neglected, while it contributes to a more significant portion in bainite. As a result, the applied load at the same indent depth is higher in bainite than in ferrite, indicating a higher hardness value. This is in consent with our observations from the L-D curves in Fig. 4.

When hydrogen is introduced, the dissolved hydrogen atoms in the matrix as interstitial solid solutes or trapped to dislocations, providing additional lattice friction on dislocation motion. Therefore, the elastoplastic regime under hydrogen-charging condition can be rewritten as

$$P = CM\alpha\mu b A_c\sqrt{\rho_{SSD} + \rho_{GND}} + C\left(\sigma_{Fric} + \sigma_{boundary} + \sigma_H\right)A_c \tag{11}$$

Where σ_H is the hydrogen-induced lattice friction. As a result, the charged hydrogen will increase the applied indenting force, indicating a hydrogen-enhanced hardness behavior.

In the current study, the charged hydrogen leads to a higher hardness value in both ferrite and bainite. However, the enhanced hardness in bainite is much higher than that in ferrite as shown in Fig. 7a. This is due to the fact that the majority of charged hydrogen exists in bainite. As a result, the hydrogen induced lattice friction σ_H in bainite is more pronounced. This can be proven from the TDS result shown in Fig. 8, which demonstrates that the total dissolved hydrogen consists of only 24.8 % diffusible hydrogen and the rest of hydrogen are in trapped condition (reversible or irreversible). From the previous studies [74,75], the diffusible hydrogen indicates the hydrogen atoms distributed into the interstitial sites, while the grain boundaries and phase boundaries can be counted as reversible trapping sites, and carbides and cementite are the examples for irreversible trapping sites. In the currently studied X65 carbon steel, the bainite contains cementite, a higher dislocation density and a smaller lath structure size. Thus, it is reasonable to deduce that most of trapping sites exist in the bainite. As a result, the diffusible hydrogen is the dominate type of hydrogen responsible for the enhanced lattice friction in ferrite, while both diffusible and trapped hydrogen are responsible for the enhanced lattice friction in bainite. If we simply assume that the diffusible hydrogen is evenly distributed in the whole microstructure and all trapped hydrogen are stored in bainite, it will indicate 12.4 % hydrogen in ferrite and 87.6 % hydrogen in bainite. Based on Eq. (11), the much higher amount of hydrogen in bainite can be used as the explanation for the more pronounced hardness increment.

5. Conclusion

In this study, the hydrogen effect on nanomechanical properties of a ferrite-bainite X65 carbon steel was examined by using the in-situ ECNI test. The elastic modulus, pop-in load, and hardness in hydrogen-free condition and hydrogen-charged condition in both microconstituents

were analyzed and discussed. The main conclusions are summarized as follows.

1. Hydrogen shows no noticeable effect on the elastic behavior in both ferrite and bainite with a constant elastic modulus regardless of hydrogen charging. The main impact of hydrogen performs on the plastic deformation.
2. The homogeneous dislocation nucleation is responsible for the pop-in phenomenon in ferrite due to its relatively low dislocation density, while the heterogeneous dislocation nucleation governs the pop-in formation in bainite owing to its higher defects content. The pop-in load in bainite is lower than that in ferrite, suggesting a lower energy barrier for heterogeneous dislocation nucleation than homogeneous dislocation nucleation. When hydrogen is introduced, the pop-in load in both microconstituents were reduced, indicating a hydrogen assisting effect on both homogeneous dislocation nucleation and heterogenous dislocation nucleation.
3. Prior to hydrogen charging, the bainite shows a higher hardness value than ferrite due to its contained cementite and dislocation-rich ferrite. During hydrogen charging, an enhanced hardness behavior was detected in both microconstituents. This phenomenon is related to the hydrogen enhanced lattice friction on dislocations. In addition, the hydrogen-enhanced hardness in bainite is more prominent than in ferrite since most of the dissolved hydrogen stays in bainite owing to its significantly more trapping sites.
4. The effect of hydrogen in each microconstituent was studied in detail. The current results raise the importance of understanding the interplay between hydrogen and the microstructures separately and optimize future pipeline engineering to obtain a better combined target property.

Data availability

The data that support the findings of this study are available on request from the corresponding author. The data are not publicly available as the data also forms part of an ongoing study.

CRediT authorship contribution statement

Dong Wang: Conceptualization, Methodology, Formal analysis, Data curation, Writing – original draft. **Anette Brocks Hagen:** Formal analysis, Writing – review & editing. **Di Wan:** Formal analysis, Writing – review & editing. **Xu Lu:** Formal analysis, Methodology, Conceptualization, Writing – review & editing. **Roy Johnsen:** Formal analysis, Writing – review & editing.

Declaration of competing interest

The authors declare that they have no known competing financial interests or personal relationships that could have appeared to influence the work reported in this paper.

Acknowledgements

The authors are grateful for the support provided by Research Council of Norway through the HyLINE (294739) and M-HEAT (294689) projects.

References

[1] M. Soudani, M. Hadj Meliani, K. El-Miloudi, Z. Azari, A.A. Sorour, N. Merah, G. Pluvinage, Reduction of hydrogen embrittlement of API 5l X65 steel pipe using a green inhibitor, Int, J. Hydrog. Energy 43 (24) (2018) 11150–11159.
[2] E. Fallahmohammadi, F. Bolzoni, L. Lazzari, Measurement of lattice and apparent diffusion coefficient of hydrogen in X65 and F22 pipeline steels, Int, J. Hydrog. Energy 38 (5) (2013) 2531–2543.
[3] Y.-H. Lee, H.M. Lee, Y.-i. Kim, S.-H. Nahm, Mechanical degradation of API X65 pipeline steel by exposure to hydrogen gas, Met. Mater. Int 17 (3) (2011) 389–395.
[4] E.S. Drexler, A.J. Slifka, R.L. Amaro, N. Barbosa, D.S. Lauria, L.E. Hayden, D. G. Stalheim, Fatigue crack growth rates of API X70 pipeline steel in a pressurized hydrogen gas environment, Fatig. Fract. Eng. Mater. Struct. 37 (5) (2014) 517–525.
[5] E. Ohaeri, U. Eduok, J. Szpunar, Hydrogen related degradation in pipeline steel: A review, Int. J. Hydrog. Energy 43 (31) (2018) 14584–14617.
[6] M.B. Djukic, V. Sijacki Zeravcic, G.M. Bakic, A. Sedmak, B. Rajicic, Hydrogen damage of steels: a case study and hydrogen embrittlement model,, Eng. Fail. Anal. 58 (2015) 485–498.
[7] I.M. Robertson, P. Sofronis, A. Nagao, M.L. Martin, S. Wang, D.W. Gross, K. E. Nygren, Hydrogen embrittlement understood, Metall. Mater. Trans. A 46a (6) (2015) 2323–2341.
[8] M. Nagumo, Hydrogen related failure of steels - a new aspect, Mater. Sci. Technol. 20 (8) (2004) 940–950.
[9] S. Lynch, Hydrogen embrittlement phenomena and mechanisms, Corrosion Rev. 30 (3–4) (2012) 105–123.
[10] D. Wang, X. Lu, D. Wan, X. Guo, R. Johnsen, Effect of hydrogen on the embrittlement susceptibility of Fe-22Mn-0.6C TWIP steel revealed by in-situ tensile tests, Mater. Sci. Eng., A 802 (2020) 140638.
[11] B. Sun, D. Wang, X. Lu, D. Wan, D. Ponge, X. Zhang, Current challenges and opportunities toward understanding hydrogen embrittlement mechanisms in advanced high-strength steels, A Review, Acta Metall. Sin. (Engl. Lett.) 34 (2021) 741–754.
[12] W.H. Johnson, On some remarkable changes produced in iron and steel by the action of hydrogen and acids, Proc. Roy. Soc. Lond. 23 (1874) 168–179.
[13] C. Beachem, A new model for hydrogen-assisted cracking (hydrogen "embrittlement"), Metall. Mater. Trans. B 3 (2) (1972) 441–455.
[14] I.M. Robertson, The effect of hydrogen on dislocation dynamics, Eng. Fract, Mech 68 (6) (2001) 671–692.
[15] P. Sofronis, I. Robertson, Transmission electron microscopy observations and micromechanical/continuum models for the effect of hydrogen on the mechanical behaviour of metals, Philos. Mag. A 82 (17-18) (2002) 3405–3413.
[16] R.A. Oriani, P.H. Josephic, Equilibrium aspects of hydrogen-induced cracking of steels, Acta Metall. 22 (9) (1974) 1065–1074.
[17] C.J. McMahon, Hydrogen-induced intergranular fracture of steels, Eng. Fract. Mech. 68 (6) (2001) 773–788.
[18] X. Lu, Y. Ma, D. Wang, On the hydrogen embrittlement behavior of nickel-based alloys: Alloys 718 and 725, Mater. Sci. Eng. A 792 (2020) 139785.
[19] X. Lu, D. Wang, D. Wan, Z.B. Zhang, N. Kheradmand, A. Barnoush, Effect of electrochemical charging on the hydrogen embrittlement susceptibility of Alloy 718, Acta Mater. 179 (2019) 36–48.
[20] A.R. Troiano, The role of hydrogen and other interstitials in the mechanical behavior of metals, Metallogr. Microstruct. Anal 5 (6) (2016) 557–569.
[21] R.B. McLellan, Z.R. Xu, Hydrogen-induced vacancies in the iron lattice, Scripta Mater. 36 (10) (1997) 1201–1205.
[22] A. Oudriss, J. Creus, J. Bouhattate, E. Conforto, C. Berziou, C. Savall, X. Feaugas, Grain size and grain-boundary effects on diffusion and trapping of hydrogen in pure nickel, Acta Mater. 60 (19) (2012) 6814–6828.
[23] A. Metsue, A. Oudriss, X. Feaugas, Hydrogen solubility and vacancy concentration in nickel single crystals at thermal equilibrium: new insights from statistical mechanics and ab initio calculations, J. Alloys Compd. 656 (2016) 555–567.
[24] R. Kirchheim, Revisiting hydrogen embrittlement models and hydrogen-induced homogeneous nucleation of dislocations, Scripta Mater. 62 (2) (2010) 67–70.
[25] R. Kirchheim, Reducing grain boundary, dislocation line and vacancy formation energies by solute segregation. I. Theoretical background, Acta Mater. 55 (15) (2007) 5129–5138.
[26] R. Kirchheim, Reducing grain boundary, dislocation line and vacancy formation energies by solute segregation II. Experimental evidence and consequences, Acta Mater. 55 (15) (2007) 5139–5148.
[27] M.B. Djukic, G.M. Bakic, V. Sijacki Zeravcic, A. Sedmak, B. Rajicic, The synergistic action and interplay of hydrogen embrittlement mechanisms in steels and iron: localized plasticity and decohesion, Eng. Fract, Mech 216 (2019) 106528.
[28] J.A. Ronevich, B.P. Somerday, C.W. San Marchi, Effects of microstructure banding on hydrogen assisted fatigue crack growth in X65 pipeline steels, Int. J. Fatig. 82 (2016) 497–504.
[29] E.V. Chatzidouros, V.J. Papazoglou, D.I. Pantelis, Hydrogen effect on a low carbon ferritic-bainitic pipeline steel, Int, J. Hydrog. Energy 39 (32) (2014) 18498–18505.
[30] E. Fallahmohammadi, F. Bolzoni, G. Fumagalli, G. Re, G. Benassi, L. Lazzari, Hydrogen diffusion into three metallurgical microstructures of a C–Mn X65 and low alloy F22 sour service steel pipelines, Int, J. Hydrog. Energy 39 (25) (2014) 13300–13313.
[31] A. Barnoush, H. Vehoff, In situ electrochemical nanoindentation: a technique for local examination of hydrogen embrittlement,, Corrosion Sci. 50 (1) (2008) 259–267.
[32] M. Zamanzade, H. Vehoff, A. Barnoush, Effect of chromium on elastic and plastic deformation of Fe3Al intermetallics, Intermetallics 41 (2013) 28–34.
[33] G. Hachet, A. Oudriss, A. Barnoush, T. Hajilou, D. Wang, A. Metsue, X. Feaugas, Antagonist softening and hardening effects of hydrogen investigated using nanoindentation on cyclically pre-strained nickel single crystal, Mater. Sci. Eng., A 803 (2020) 140480.
[34] T. Depover, D. Wan, D. Wang, A. Barnoush, K. Verbeken, The effect of hydrogen on the crack initiation site of TRIP-assisted steels during in-situ hydrogen plasma micro-tensile testing: leading to an improved ductility?, Mater, Character 167 (2020) 110493.

[35] D. Wang, X. Lu, Y. Deng, D. Wan, Z. Li, A. Barnoush, Effect of hydrogen-induced surface steps on the nanomechanical behavior of a CoCrFeMnNi high-entropy alloy revealed by in-situ electrochemical nanoindentation, Intermetallics 114 (2019) 106605.
[36] D. Wang, X. Lu, D. Wan, Z. Li, A. Barnoush, In-situ observation of martensitic transformation in an interstitial metastable high-entropy alloy during cathodic hydrogen charging, Scripta Mater. 173 (2019) 56–60.
[37] X. Lu, Y. Ma, M. Zamanzade, Y. Deng, D. Wang, W. Bleck, W.W. Song, A. Barnoush, Insight into hydrogen effect on a duplex medium-Mn steel revealed by in-situ nanoindentation test, Int, J. Hydrog. Energy 44 (36) (2019) 20545–20551.
[38] A. Barnoush, H. Vehoff, Recent developments in the study of hydrogen embrittlement: hydrogen effect on dislocation nucleation, Acta Mater. 58 (16) (2010) 5274–5285.
[39] A. Barnoush, A. Basa, C. Thaulow, Oxygen argon plasma treatment effect on hydrogen uptake in austenitic stainless steels, Int, J. Hydrog. Energy 39 (26) (2014) 14120–14131.
[40] X. Lu, D. Wang, Effect of hydrogen on deformation behavior of Alloy 725 revealed by in-situ bi-crystalline micropillar compression test, J. Mater. Res. Technol 67 (2021) 243–253.
[41] X. Lu, D. Wang, Z. Li, Y. Deng, A. Barnoush, Hydrogen susceptibility of an interstitial equimolar high-entropy alloy revealed by in-situ electrochemical microcantilever bending test, Mater. Sci. Eng., A 762 (2019) 138114.
[42] S. Zaefferer, N.N. Elhami, Theory and application of electron channelling contrast imaging under controlled diffraction conditions, Acta Mater. 75 (2014) 20–50.
[43] K.L. Johnson, Contact Mechanics, Cambridge University Press, Cambridge, 1987.
[44] S. Lee, A. Vaid, J. Im, B. Kim, A. Prakash, J. Guenole, D. Kiener, E. Bitzek, S.H. Oh, In-situ observation of the initiation of plasticity by nucleation of prismatic dislocation loops, Nat. Commun. 11 (1) (2020).
[45] K. Gan, D. Yan, S. Zhu, Z. Li, Interstitial effects on the incipient plasticity and dislocation behavior of a metastable high-entropy alloy: nanoindentation experiments and statistical modeling, Acta Mater. 206 (2021) 116633.
[46] S. Jiapeng, L. Cheng, J. Han, A. Ma, L. Fang, Nanoindentation induced deformation and pop-in events in a silicon crystal: molecular dynamics simulation and experiment, Sci. Rep. 7 (1) (2017).
[47] W.C. Oliver, G.M. Pharr, Measurement of hardness and elastic modulus by instrumented indentation: advances in understanding and refinements to methodology, J. Mater. Res. 19 (1) (2004) 3–20.
[48] D. Pérez Escobar, T. Depover, L. Duprez, K. Verbeken, M. Verhaege, Combined thermal desorption spectroscopy, differential scanning calorimetry, scanning electron microscopy and X-ray diffraction study of hydrogen trapping in cold deformed TRIP steel, Acta Mater. 60 (6–7) (2012) 2593–2605.
[49] D. Wang, X. Lu, Y. Deng, X. Guo, A. Barnoush, Effect of hydrogen on nanomechanical properties in Fe-22Mn-0.6C TWIP steel revealed by in-situ electrochemical nanoindentation, Acta Mater. 166 (2019) 618–629.
[50] S. Qu, X. Pang, Y. Wang, K. Gao, Corrosion behavior of each phase in low carbon microalloyed ferrite–bainite dual-phase steel: experiments and modeling, Corrosion Sci. 75 (2013) 67–77.
[51] L. Ligang, X. Hong, L. Qiang, L. Yu, L. Peishuai, Y. Zhiqiang, Y. Hui, Evaluation of the fracture toughness of X70 pipeline steel with ferrite-bainite microstructure, Mater. Sci. Eng., A 688 (2017) 388–395.
[52] V. Shalskyi, Z. Nazarchuk, S. Hirnyi, Effect of electrolytically absorbed hydrogen on Young's modulus of structural steel, Mater. Sci. 48 (4) (2013) 491–499.
[53] K. Tomatsu, K. Miyata, T. Omura, Electrochemical nanoindentation study on influence of hydrogen on local mechanical properties of Fcc metals at slow strain rate, ISIJ Int. 56 (3) (2016) 418–423.
[54] T.-Y. Zhang, F.-X. Jiang, W.-Y. Chu, C.-M. Hsiao, Effect of hydrogen on the Young's modulus of iron, Metall. Trans. A 16 (9) (1985) 1655–1662.
[55] E. Lunarska, A. Zielinski, M. Smialowski, Effect of hydrogen on shear modulus of polycrystalline alpha-iron, Acta Metall. 25 (3) (1977) 305–308.
[56] C. Müller, M. Zamanzade, C. Motz, The impact of hydrogen on mechanical properties; A new in situ nanoindentation testing method, Micromachines 10 (2) (2019) 114.
[57] M. Ortiz, J. Ovejero-Garcia, Effect of hydrogen on Young's modulus of AISI 1005 and 1070 steels, J. Mater. Sci. 27 (24) (1992) 6777–6781.
[58] T.-H. Ahn, S.B. Lee, K.-T. Park, K.H. Oh, H.N. Han, Strain-induced ε-martensite transformation during nanoindentation of high-nitrogen steel, Mater. Sci. Eng., A 598 (2014) 56–61.
[59] N.G. Chechenin, J. Bøttiger, J.P. Krog, Nanoindentation of amorphous aluminum oxide films II. Critical parameters for the breakthrough and a membrane effect in thin hard films on soft substrates, Thin Solid Films 261 (1) (1995) 228–235.
[60] Y. Zhao, J.-M. Park, J.-i Jang, U. Ramamurty, Bimodality of incipient plastic strength in face-centered cubic high-entropy alloys, Acta Mater. 202 (2021) 124–134.
[61] D. Wang, X. Lu, M. Lin, D. Wan, Z. Li, J. He, J. Roy, Understanding the hydrogen effect on pop-in behavior of an equiatomic high-entropy alloy during in-situ nanoindentation, J. Mater. Res. Technol 98 (2021) 118–122.
[62] J. Frenkel, Zur Theorie der Elastizitätsgrenze und der Festigkeit kristallinischer Körper 37 (7) (1926) 572–609.
[63] D. Wu, T.G. Nieh, Incipient plasticity and dislocation nucleation in body-centered cubic chromium, Mater. Sci. Eng., A 609 (2014) 110–115.
[64] P.M. Anderson, J.P. Hirth, J. Lothe, Theory of Dislocations, third ed., Cambridge University Press, Cambridge, 2017.
[65] C. Zhu, Z.P. Lu, T.G. Nieh, Incipient plasticity and dislocation nucleation of FeCoCrNiMn high-entropy alloy, Acta Mater. 61 (8) (2013) 2993–3001.
[66] S. Izumi, S. Yip, Dislocation nucleation from a sharp corner in silicon, J. Appl. Phys. 104 (3) (2008) 33513.
[67] H. Bei, Y.F. Gao, S. Shim, E.P. George, G.M. Pharr, Strength differences arising from homogeneous versus heterogeneous dislocation nucleation, Phys. Rev. B 77 (6) (2008).
[68] H. Yu, A. Cocks, E. Tarleton, Discrete dislocation plasticity HELPs understand hydrogen effects in bcc materials, J. Mech. Phys. Solid. 123 (2019) 41–60.
[69] G. Yang, Y. Zhao, D.-H. Lee, J.-M. Park, M.-Y. Seok, J.-Y. Suh, U. Ramamurty, J.-I. Jang, Influence of hydrogen on incipient plasticity in CoCrFeMnNi high-entropy alloy, Scripta Mater. 161 (2019) 23–27.
[70] I. Salehinia, D.F. Bahr, The impact of a variety of point defects on the inception of plastic deformation in dislocation-free metals, Scr. Mater 66 (6) (2012) 339–342.
[71] S. Mukherjee, T. Khraishi, Y.L. Shen, Modeling the effects of particles, interstitials, vacancies and tip geometry on indentation-induced plasticity, Mol. Simulat. 32 (8) (2006) 651–656.
[72] B.-W. Choi, D.-H. Seo, J.-Y. Yoo, J.-i. Jang, Predicting macroscopic plastic flow of high-performance, dual-phase steel through spherical nanoindentation on each microphase, J. Mater. Res. 24 (3) (2009) 816–822.
[73] W.D. Nix, H.J. Gao, Indentation size effects in crystalline materials: a law for strain gradient plasticity, J. Mech. Phys. Solids 46 (3) (1998) 411–425.
[74] D.P. Escobar, K. Verbeken, L. Duprez, M. Verhaege, Evaluation of hydrogen trapping in high strength steels by thermal desorption spectroscopy, Mater. Sci. Eng., A 551 (2012) 50–58.
[75] K. Bergers, E.C. de Souza, I. Thomas, N. Mabho, J. Flock, Determination of hydrogen in steel by thermal desorption mass spectrometry, steel res, Bar Int. 81 (7) (2010) 499–507.